

Aerodynamic analysis of an unmanned aerial vehicle with infrared camera for monitoring oil leakage in pipeline networks

Análisis aerodinámico de un vehículo aéreo no tripulado con cámara infrarroja para monitorear fugas de hidrocarburos en redes de oleoductos

Ernesto A. Elvira-Hernández¹, Francisco López-Huerta², Héctor Vázquez-Leal³,
Quetzalcoatl Hernández-Escobedo⁴, Agustín L. Herrera-May^{1,5*}

¹Micro and Nanotechnology Research Center, Universidad Veracruzana, Calzada Ruiz Cortines 455, Boca del Río, Veracruz, México. C.P. 94294.

²Facultad de Ingeniería Eléctrica y Electrónica, Universidad Veracruzana.

³Facultad de Instrumentación Electrónica, Universidad Veracruzana.

⁴Escuela Nacional de Estudios Superiores Juriquilla, Universidad Nacional Autónoma de México, Querétaro, México. C.P. 76230.

⁵Maestría en Ingeniería Aplicada, Facultad de Ingeniería de la Construcción y el Hábitat, Universidad Veracruzana, Calzada Ruiz Cortines 455, Boca del Río, Veracruz 94294, México.

*Corresponding author: leherrera@uv.mx

Abstract

Oil pipeline networks require periodic inspection to detect damages that can generate oil leakage in natural and human environments. These damages can be caused by geological hazard and interference from third party. In order to detect these damages, low-cost techniques that consider both the oil pipeline networks and the environment are required. In this paper, the aerodynamic analysis of an unmanned aerial vehicle (UAV) with Eppler 748 sailplane airfoil (wingspan of 1.635 m) is presented. The UAV can include a small infrared camera for monitoring oil leakage of a pipeline network using the infrared radiation related to oil. A computational fluid dynamics (CFD) model of the UAV is developed to predict its lift and drag coefficients as a function of the Reynolds number and the angle of attack (AoA). The air velocity profile around UAV is estimated with the CFD simulations. In addition, a scale model (1:6.5) of the UAV is fabricated using a 3D printer, which is tested employing a subsonic wind tunnel. For the UAV with AoA of 0°, the drag and lift coefficients obtained with the CFD model have a similar behavior with respect to those measured through the subsonic wind tunnel. The designed UAV could be used for low-cost inspections of damages in oil pipeline networks in comparison with the use of helicopters or light aircraft.

Keywords: Aerodynamic analysis; computational fluid dynamics; drag coefficient; infrared camera; lift coefficient; unmanned aerial vehicle.

Resumen

Las redes de oleoductos requieren inspección periódica para detectar daños que pueden causar fugas de hidrocarburos en ambientes naturales y en poblaciones humanas. Estos daños pueden ser causados por fenómenos geológicos e interferencia de seres humanos. Para la detección de estos daños son necesarios técnicas de bajo costo que consideren las redes de oleoductos y su entorno natural. Este estudio presenta un análisis aerodinámico de un vehículo aéreo no tripulado (UAV) con perfil aerodinámico Eppler 748 (longitud del ala de 1.635 m). El UAV puede incluir una pequeña cámara infrarroja para monitorear fugas de hidrocarburos en redes de oleoductos usando la radiación infrarroja relacionada con el hidrocarburo derramado. Un modelo de dinámica de fluidos computacional (CFD) de el UAV es desarrollado para predecir sus coeficientes de sustentación y arrastre como una función del número de Reynolds y el ángulo de ataque (AoA). El perfil de velocidad del aire alrededor del UAV es estimado con simulaciones de CFD. Además, un modelo a escala (1:6.5) del UAV es fabricado usando una impresora 3D para realizar pruebas experimentales con un túnel de viento subsónico. Para el UAV con un AoA de 0°, los coeficientes de sustentación y arrastre obtenidos con el modelo CFD tienen un comportamiento similar con los medidos a través del túnel de viento subsónico. El UAV diseñado podría utilizarse para inspecciones de bajo costo en redes de oleoductos en comparación con el empleo de helicópteros y aviones ligeros.

Palabras clave: Análisis aerodinámico; dinámica de fluidos computacional; coeficiente de arrastre; cámara infrarroja; coeficiente de sustentación; vehículo aéreo no tripulado.

Recibido: 03 de marzo de 2019

Aceptado: 10 de enero de 2020

Publicado: 12 de febrero de 2020

Como citar: Elvira-Hernández, E. A., López-Huerta, F., Vázquez-Leal, H., Hernández-Escobedo, Q., Herrera-May, A. L. (2020). Aerodynamic analysis of an unmanned aerial vehicle with infrared camera for monitoring oil leakage in pipeline networks. *Acta Universitaria* 30, e2534. doi. <http://doi.org/10.15174/au.2020.2534>

Introduction

The oil industry uses pipeline networks to transport oil through thousands of kilometers. Generally, these pipeline networks are built from steel and cast iron, which need regular inspections. These inspections are required to detect pipeline failures that can cause oil leakage with long-term and irreversible impacts in natural and human environments (Gómez & Green, 2017; Rifai, Abdalla, Razali, Ali & Faraj, 2017; Shu-Jiao, Zong-Zhi, Ru-Jun & Hao, 2016). These oil pipeline failures can be generated by corrosion, cracks, geological hazard, interference from a third party, incorrect operations and inappropriate design (Barros, 2016; Guo *et al.*, 2016; Iqbal, Tesfamariam, Haider & Sadiq, 2016; Liang, Hu, Zhang, Guo & Lin, 2012; Mohamed, Hamdi & Tahar, 2017; Yuhua & Datao, 2005; Zhou, Wu, Liu, Li & Qiao, 2016). The main technique used for monitoring these types of failure includes smart pigs (Lima, Freitas, Araújo, Maitelli & Salazar, 2017; Rodríguez-Olivares *et al.*, 2018; Sahli & El-Sheimy, 2016). The smart pigs contain sensors mounted on a mechanical system that moves within the oil pipes. These sensors can detect cracks and corrosion on the internal surface of the pipes. However, this technique is expensive, and it is not suitable for the detection of oil pipeline damages generated by external sources such as floods, vandalism and illegal oil theft. For these cases, it is necessary to use alternative low-cost techniques that consider both the pipelines and the environment. In addition, these novel techniques require the real-time detection of oil leakage along the pipeline networks. An alternative technique for monitoring oil leakage in pipeline networks is using an unmanned aerial vehicle (UAV) with an infrared camera, which could take images of the infrared radiation related to the oil. By using a global positioning system (GPS) and communication systems, the UAV could send infrared images to a control center in real-time. For this, UAV require to keep a suitable aerodynamic stability coupled with a low drag coefficient. The aerodynamic analysis of the UAV can be done using computational fluid dynamics (CFD) and tests in wind tunnels. Several researchers (Bravo-Mosquera, Botero-Bolivar, Acevedo-Giraldo & Cerón-Muñoz, 2017; Du, Dori, Divo, Huayamave & Zhu, 2018; Jung-Ryul *et al.*, 2015; Panagiotou, Fotiadis-Karras & Yakinthos, 2018; Pangiotou, Kaparos, Salpingidou & Yakinthos, 2016; Panagiotou, Loannidis, Tzivinikos & Yakinthos, 2017; Raeisi & Alighanbari, 2018; Shen, Su, Liang & Zhu, 2018; Shukla & Komerath, 2018; Sóbester, Keane, Scanlan & Bressloff, 2005; Yang, Xue, Cai, Sun & Zhou, 2018) have developed aerodynamic studies of UAV using CFD and tests in wind tunnels; however, most of these UAV do not include the effect of an infrared camera on their outer surface. Thus, the aerodynamic analysis of a UAV with an infrared camera is presented in this research. This design could decrease the inspection costs with respect to techniques that include helicopters and light aircrafts. Furthermore, the UAV design includes winglets to achieve a stable flight during its trajectory along the pipeline network. To determine the aerodynamic parameters of the UAV, CFD models through the ANSYS software are developed. In addition, a scaled model (1:6.5) of the UAV is fabricated employing a 3D printer, which is tested using a subsonic wind tunnel. The drag and lift coefficients determined with CFD models have good agreement with respect to those measured using the subsonic wind tunnel. The winglets of the UAV allow the reduction of vortices and increase the lift force, improving the UAV stability.

This study is structured as follows: Section 2 describes the CFD modeling of the UAV; Section 3 shows the experimental setup; Section 4 depicts the results and discussion related with lift and drag coefficients of the UAV determined with the CFD models and experimental tests; and Section 5 includes the conclusions and future research.

CFD modeling

Figure 1 shows the UAV design that considers a wing (1250 mm × 200 mm) with Eppler 748 sailplane airfoil, two winglets at the wing ends and an infrared camera. Figure 2 depicts the dimensions of the UAV, considering the infrared camera and winglets. The oil leakage in pipeline networks could cause changes

in the ground temperature, altering its infrared radiation emission. A GPS and a communication system of the UAV will allow a real-time transmission of these images.

This UAV can be built using expanded polypropylene (EPP), which is light-weight and low cost (Bouix, Viot & Lataillade, 2009; Frederick *et al.*, 1995). Table 1 indicates the main mechanical properties of the EPP. To increase the stiffness of the UAV, an airframe is fabricated using commercial aluminum tubes with an outer diameter of 7.93 mm and thickness of 1 mm (figure 3). The weight of the main components of the UAV airframe is described in table 2. This data is used to estimate the gravity center of the UAV (figure 4). The total weight of the UAV is calculated considering the payload weight (infrared camera, batteries, motors and electronic components) and empty weight (airframe). To achieve the flight of the UAV, the lift force must be higher than the total weight (21.07 N) of the UAV.

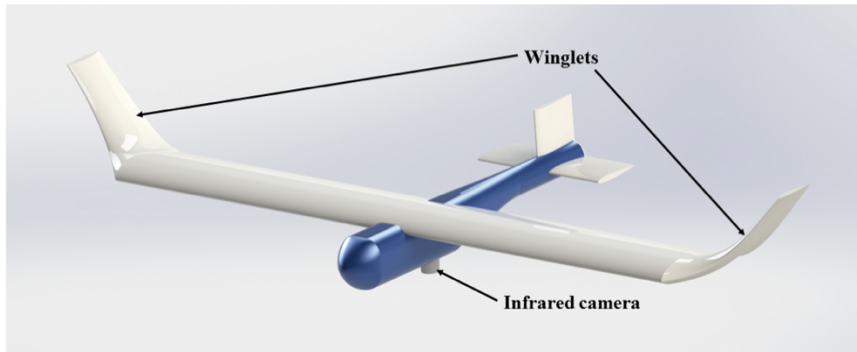


Figure 1. 3D view of the UAV design with an infrared camera and winglets in the wing ends.
Source: Author's own elaboration.

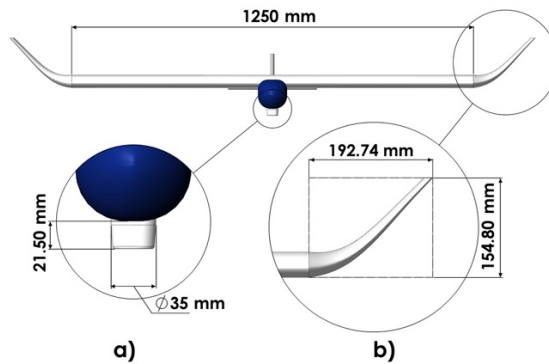


Figure 2. Dimensions of wing, a) infrared camera and b) winglets of the UAV.
Source: Author's own elaboration.

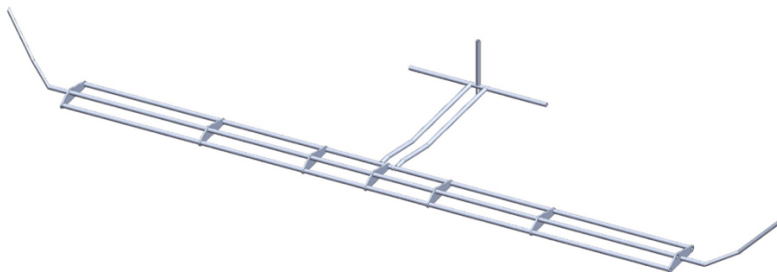


Figure 3. Airframe of the UAV formed by aluminum tubes.
Source: Author's own elaboration.

Table 1. Mechanical properties of EPP foam for different densities (Frederick *et al.*, 1995).

Mechanical properties	Density (kg/m ³)			
	20	44	60	80
Young's modulus (MPa)	75	215	320	470
Poisson ratio	0.00	0.03	0.04	0.03
Yield strength (MPa)	2.4	7.7	10.0	14.1

Source: Author's own elaboration.

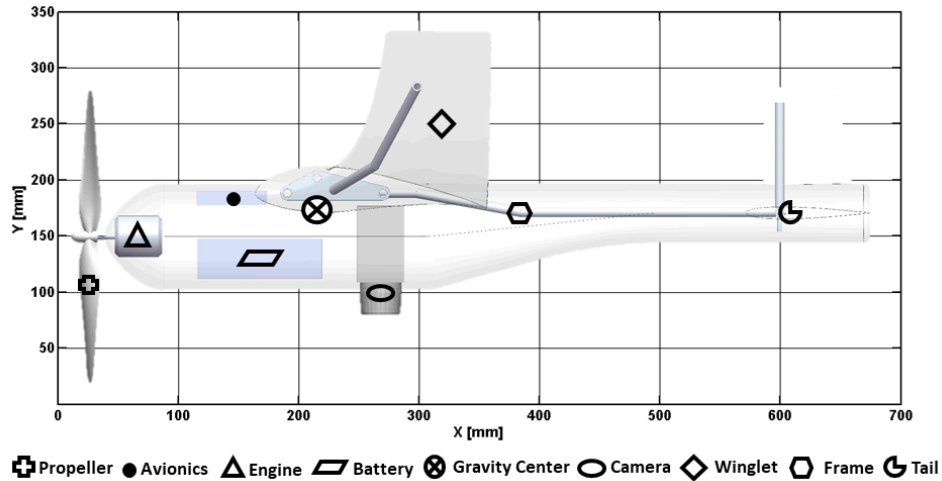


Figure 4. Schematic view of the gravity center of internal components of the UAV.

Source: Author's own elaboration.

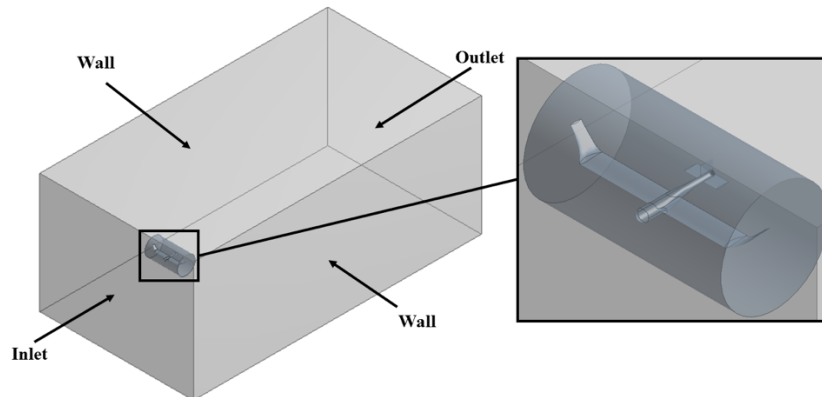


Figure 5. CAD geometry and boundary conditions of the UAV CFD model.

Source: Author's own elaboration.

Table 2. Weight of the main components of the UAV design.

Component	Weight (N)
Propeller	0.332
Avionics	2.943
Engine	1.540
Battery	3.188
Camera	1.962
Fuselage	7.406
Frame	3.708
Total	21.07

Source: Author's own elaboration.

A CFD model was developed using the ANSYS®-CFX software (ANSYS Inc, 2019) to predict the aerodynamic behavior of the UAV. First, the geometry of the UAV model using a CAD software (SolidWorks®) was elaborated, as shown in figure 5. In this CAD model, the infrared camera is considered, but the propeller of the UAV was negligible. Next, this CAD model is exported to ANSYS®-CFX software and is meshed using tetrahedral elements. For the aerodynamic analysis, a control volume of the fluid is developed. The four walls (top, bottom and sides) of the control volume and the outer surface of the UAV model are evaluated as free slip walls (ideal walls) and as no slip walls, respectively. The temperature and air pressure are determined as 25 °C and 1 atm, respectively. With these values, the numerical simulations and experimentation were conducted; however, the UAV could fly in colder or warmer conditions. The changes in air temperature can affect its density, which will alter the values of the drag and lift coefficients of the UAV. The shear stress transport (SST) turbulence model is employed because it is suitable for geometries with curvature profiles and aerodynamic applications (Menter, Kuntz & Langtry, 2003). In the CFD simulation, a steady state flow is considered. In addition, in the inlet volume is estimated a subsonic flow regime with a velocity range between 1 m/s to 26 m/s and a turbulence intensity of 5%. Also, in the outlet surface is specified a relative pressure of 0 Pa.

The SST model contained in ANSYS-CFX software is based on the turbulence model reported by Menter (1993) (Bardina, Huang & Coakley, 1997; Menter, Carregal-Ferreira, Esch & Konno, 2003; Menter *et al.*, 2003). This SST model employs the best elements of the $k - \epsilon$ turbulence model and $k - \omega$ turbulence model by means of a blending function F_1 . This function has as value of 1 near the wall surface and 0 in the free shear flows and outer part. With these magnitudes of F_1 , in the near-wall surface is activated the $k - \omega$ model; conversely, for the rest of the flow is employed the $k - \epsilon$ model. Thus, the SST model uses the two-equation of the $k - \omega$ model near the wall surface and the $k - \epsilon$ model in the rest of the flow. The SST model is suitable for aeronautics flows with high adverse pressure gradients and separation. The SST model uses equations for the turbulent kinetic energy (k) and the turbulence frequency (ω), which can be determined by (Menter *et al.*, 2003):

$$\frac{\partial(\rho k)}{\partial t} + \frac{\partial(\rho U_i k)}{\partial x_i} = \tilde{P}_k - \beta^* \rho k \omega + \frac{\partial}{\partial x_i} \left[(\mu + \sigma_k \mu_t) \frac{\partial k}{\partial x_i} \right] \quad (1)$$

$$\frac{\partial(\rho \omega)}{\partial t} + \frac{\partial(\rho U_i \omega)}{\partial x_i} = \alpha \rho S^2 - \beta \rho \omega^2 + \frac{\partial}{\partial x_i} \left[(\mu + \sigma_\omega \mu_t) \frac{\partial \omega}{\partial x_i} \right] + 2(1 - F_1) \rho \sigma_{\omega 2} \frac{1}{\omega} \frac{\partial k}{\partial x_i} \frac{\partial \omega}{\partial x_i} \quad (2)$$

with

$$F_1 = \tanh \left\{ \left\{ \min \left[\max \left(\frac{\sqrt{k}}{\beta^* \omega y}, \frac{500\nu}{y^2 \omega} \right), \frac{4\rho \sigma_{\omega 2} k}{CD_{k\omega} y^2} \right] \right\}^4 \right\} \quad (3)$$

$$CD_{k\omega} = \max \left(2\rho \sigma_{\omega 2} \frac{1}{\omega} \frac{\partial k}{\partial x_i} \frac{\partial \omega}{\partial x_i}, 10^{-10} \right) \quad (4)$$

where t is the time; μ is the fluid viscosity; ρ is the fluid density; k is the turbulent kinetic energy; x_i is the space coordinate component; $i, \alpha, \sigma_k, \beta, \beta^*$ and σ_ω are model constants; ω is the turbulence frequency; U_i is the mean flow velocity component in the x_i coordinate direction; ν is the kinematic viscosity; S is the magnitude of the mean vorticity; and y is the distance to the nearest wall surface.

The turbulent eddy viscosity (μ_t) is given by:

$$\mu_t = \frac{a_1 k}{\max(a_1 \omega, S F_2)} \quad (5)$$

$$F_2 = \tanh \left[\left[\max \left(\frac{2\sqrt{k}}{\beta^* \omega y}, \frac{500\nu}{y^2 \omega} \right) \right]^2 \right] \quad (6)$$

$$\bar{P}_k = \min(P_k, 10\beta^* \rho k \omega) \quad (7)$$

$$P_k = \mu_t \frac{\partial U_i}{\partial x_j} \left(\frac{\partial U_i}{\partial x_j} + \frac{\partial U_j}{\partial x_i} \right) \quad (8)$$

where a_1 is a constant and F_2 is a second blending function.

The SST model coefficients α, β, σ_k and σ_ω , described with the symbol ϕ , are indicated by blending the coefficients of the original $k - \omega$ model, named as ϕ_1 , through those of the converted $k - \varepsilon$ model, called as ϕ_2 :

$$\phi = F_1 \phi_1 + (1 - F_1) \phi_2 \quad (9)$$

$$\phi = (\sigma_k, \sigma_\omega, \beta, \alpha) \quad (10)$$

The constants used in the SST model are: $\beta^* = 0.09, \alpha_1 = 5/9, \beta_1 = 3/40, \sigma_{k1} = 0.85, \sigma_{\omega1} = 0.5, \alpha_2 = 0.44, \beta_2 = 0.0828, \sigma_{k2} = 1,$ and $\sigma_{\omega2} = 0.856$ (Menter *et al.*, 2003).

For the mesh of the UAV CFD model, it is necessary to calculate the distance between the first layer of the mesh and the UAV outer surface. This distance (Δs) is given by (Schlichting & Garsten, 2017):

$$\Delta s = \frac{\mu y^+}{\rho U^*} \quad (11)$$

where y^+ is a dimensionless parameter that depends on the turbulence model and U^* is the fluid velocity when it has contact with the UAV geometry.

Based on equation (11), a fine mesh is implemented around the first layers of the outer surface of the UAV. The characteristic length (L_c) of the UAV can be calculated using a rectangular section (a width and b thickness) (Cengel, 2014):

$$L_c = \frac{2ab}{a+b} \quad (12)$$

The shear stress around the UAV outer surface can be estimated as (Schlichting & Garsten, 2017):

$$\tau_w = \frac{1}{2} C_f \rho U^2 \quad (13)$$

$$C_f = [2 \log(Re) - 0.65]^{-2.3} \quad (14)$$

where U is the fluid velocity, C_f is the friction coefficient of the UAV outer surface and Re is the Reynolds number.

The fluid velocity (U^*) around the UAV outer surface is obtained as (Schlichting & Garsten, 2017):

$$U^* = \sqrt{\frac{\tau_w}{\rho}} \quad (15)$$

The magnitude of y^+ can be calculated by (Menter *et al.*, 2003):

$$y^+ = \frac{u}{U^*} \quad (16)$$

Experimental setup

Experimental measurements of the lift and drag coefficients of the UAV are developed using a TecQuipment AF100 open circuit subsonic wind tunnel (figure 6). This tunnel has a test section with dimensions of 0.30 m × 0.30 m × 0.60 m.

This tunnel has an aerodynamic balance that measures the lift and drag forces. For the experimental test, the UAV wing is scaled from 1.635 m to 0.25 m using a 3D printer. This 3D UAV model is supported through a circular bar with 12.7 mm diameter and 200 mm length. Thus, the UAV is connected to the aerodynamic balance of the aerodynamic tunnel (figure 7).



Figure 6. TecQuipment AF100 subsonic wind tunnel used in the aerodynamic test of the 3D UAV model.
Source: Author's own elaboration.

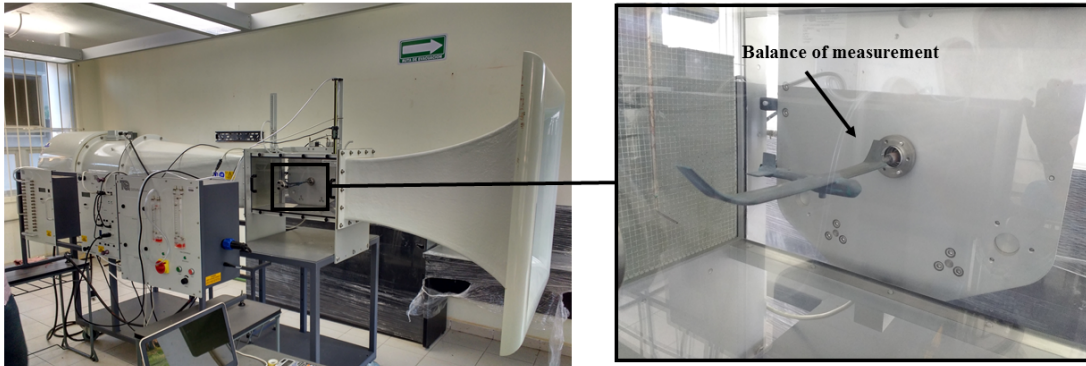


Figure 7. 3D UAV model used in the TecQuipment AF100 subsonic wind tunnel.
Source: Author's own elaboration.

In the experimental test, a similitude criterion is used to obtain the velocities relation between the 3D UAV model and UAV CFD model. For this criterion, the 3D UAV model and UAV CFD model have equal Reynolds number. Table 3 shows the velocities relations between the 3D UAV model and UAV CFD model (Munson, Okishi, Rothmayer & Huebsch, 2009). The maximum velocity that can be reached in the wind tunnel test chamber is 36 m/s. This velocity in the model corresponds to approximately 5.5 m/s in the real-size prototype.

$$V_m = \frac{\mu_m \rho}{\mu \rho_m} \frac{l}{l_m} V \quad (17)$$

where V_m , μ_m , ρ_m , l_m , V , μ , ρ and l are the velocity, dynamic viscosity, density and characteristic length in the model, and prototype, respectively.

Table 3. Velocities' relations between the 3D UAV model and UAV CFD model.

Prototype velocity (m/s)	Model velocity (m/s)
4.0	26.1
4.5	29.3
5.0	32.6
5.5	35.8

Source: Author's own elaboration.

Results and discussion

In the UAV CFD simulations, an air velocity range that goes from 1 m/s to 26 m/s (Reynolds number from 27759 to 721741) is considered, keeping an angle of attack (AoA) of 0°. Figures 8 (a-b) depict the drag coefficient and drag force of the UAV CFD model as function of its Reynold number. The drag forces have an important increment when the velocity increases, while the drag coefficient decreases under the same conditions. The maximum values of the drag coefficient and drag force are 0.0234 N and 7.56 N, respectively, with wind velocities of 26 m/s (Re = 721741).

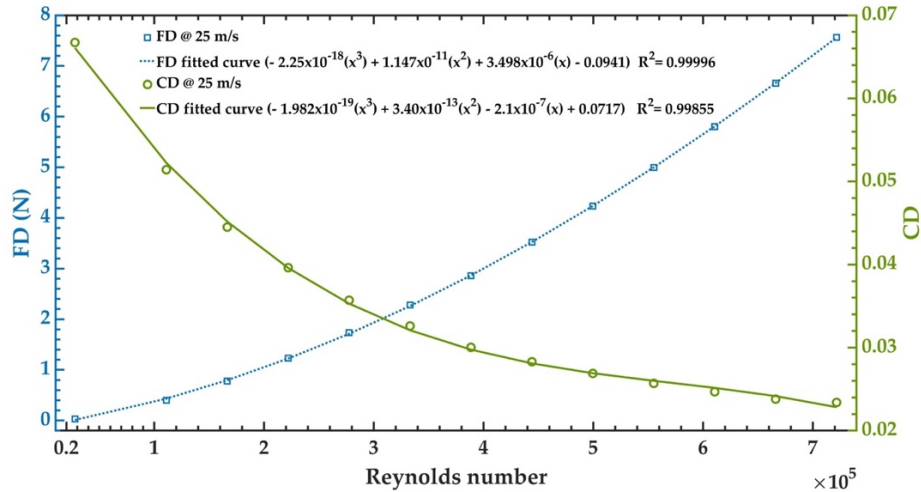


Figure 8. Drag force and drag coefficient of the UAV CFD model vs. its Reynolds number.
Source: Author's own elaboration.

Apart from that, the force and lift coefficient increase as the wind velocity increases (figure 9). The maximum values of the coefficient and lift force are 0.2294 N and 68.93 N, respectively, with wind speed of 26 m/s ($Re = 721741$). In other UAV CFD simulations, the AoA is changed between 0° and 20° , keeping a constant inlet velocity of 26 m/s. Figure 10 depicts the lift force and lift coefficient of the UAV as a function of AoA. Lift force and lift coefficient increases when AoA varies between 0° and 18° . Thus, the maximum value (203 N) of the lift force and lift coefficient (0.6684) is achieved with AoA of 18° and decay for AoA higher than 18° . However, these values are decreased for AoA higher than 18° . Figure 11 shows the drag force and drag coefficient as a function of AoA. The values of these aerodynamic parameters are increased when the AoA of the vehicle is incremented.

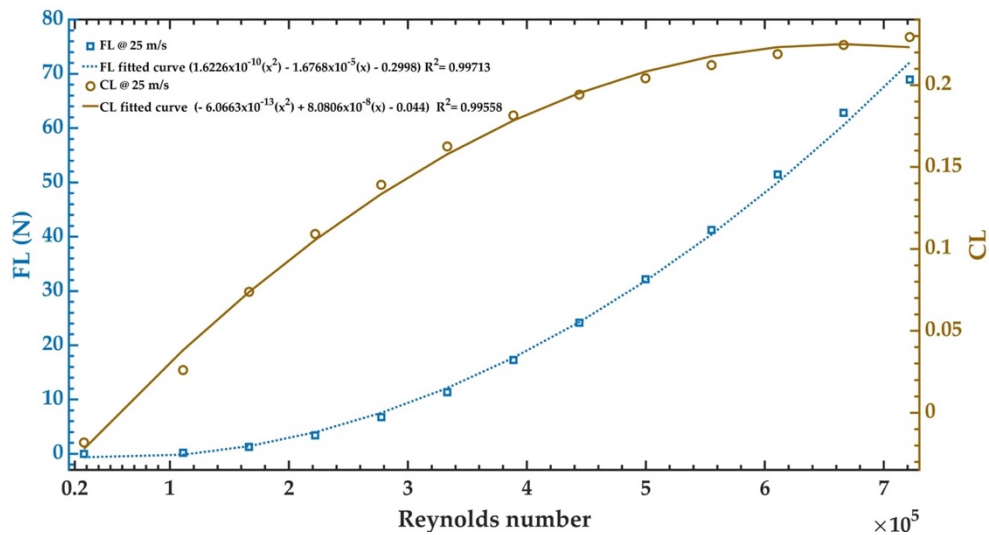


Figure 9. Lift force and lift coefficient of the UAV CFD model vs. its Reynolds number.
Source: Author's own elaboration.

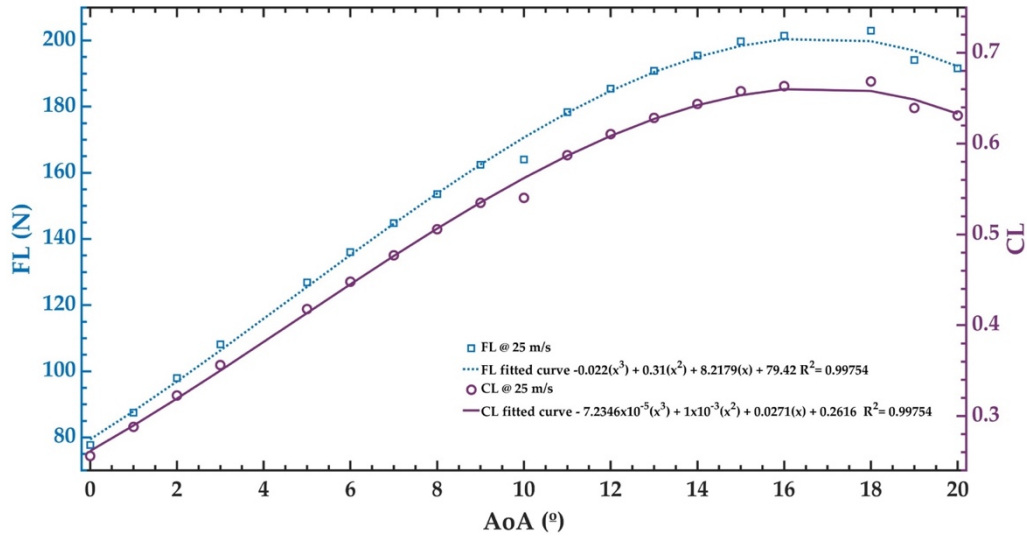


Figure 10. Lift force and lift coefficient of the UAV CFD model vs. AoA.
Source: Author's own elaboration.

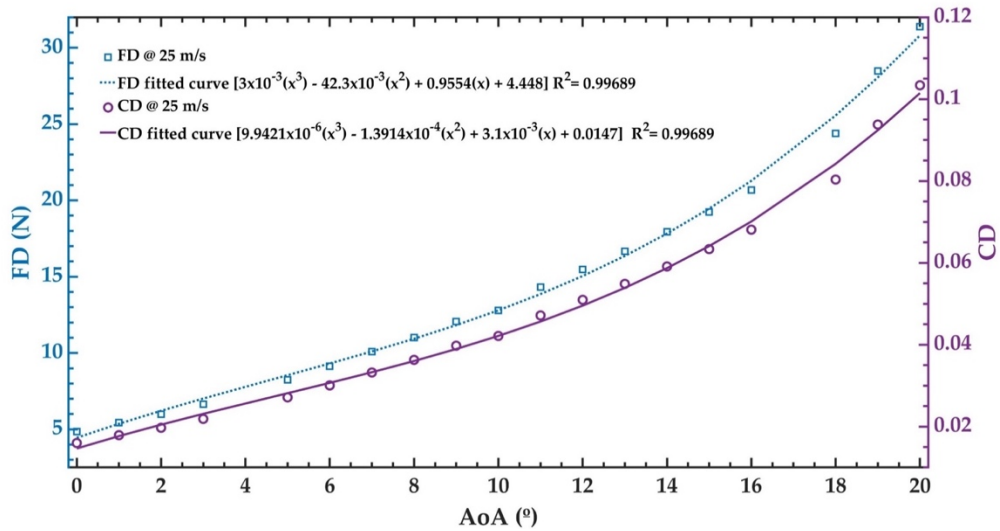


Figure 11. Drag force and drag coefficient of the UAV CFD model vs. AoA.
Source: Author's own elaboration.

Figure 12 and 13 show the air velocity profile about the surface of the UAV CFD model. For this aerodynamic design, the UAV registers a uniform velocity profile. Moreover, the winglets allow the reduction of air turbulence at the wing ends.

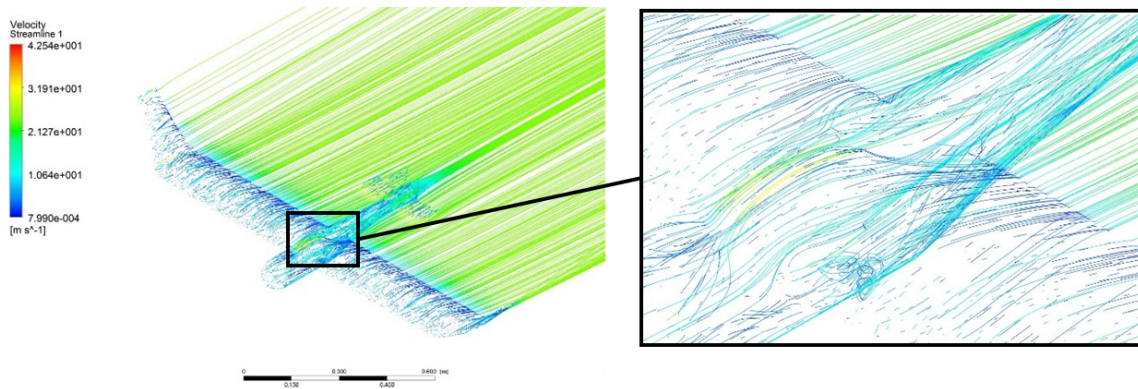


Figure 12. Air velocity profile about the surface of the UAV CFD model.
Source: Author's own elaboration.

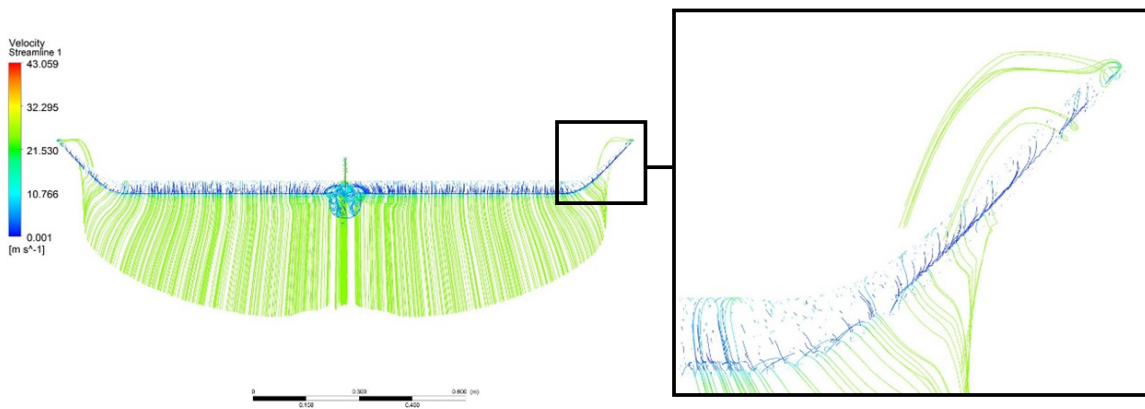


Figure 13. Air velocity profile around the winglets of the UAV CFD model.
Source: Author's own elaboration.

Figure 14 shows the experimental response of the lift coefficients of the 3D UAV model. The experimental values of the lift coefficients increment when the Reynolds number increases. The maximum and minimum magnitudes of the lift coefficients are 0.08 and 0.003, respectively. On the other hand, figure 15 illustrates the experimental results of the drag coefficients of the 3D UAV model. The maximum and minimum values of the drag coefficients are 0.050 and 0.040, respectively. The drag coefficients obtained with the UAV CFD model have a similar response in comparison with those measured using the wind tunnel. Nevertheless, the lift coefficients of the UAV CFD model registered magnitudes smaller than those measured through the wind tunnel.

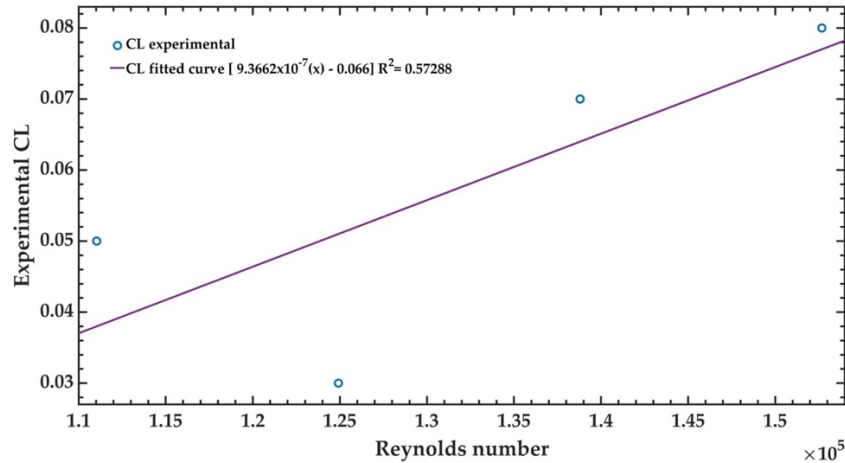


Figure 14. Experimental lift coefficient of the 3D UAV model using the TecQuipment AF100 subsonic wind tunnel.
Source: Author's own elaboration.

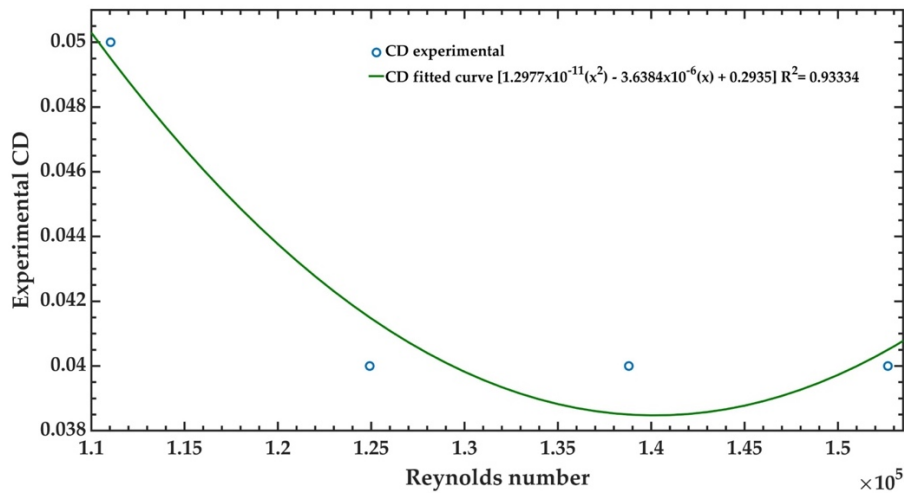


Figure 15. Experimental drag coefficient of the 3D UAV model using the TecQuipment AF100 subsonic wind tunnel.
Source: Author's own elaboration.

Conclusions

An aerodynamic analysis of an UAV model with Eppler 748 sailplane airfoil (wingspan of 1.635 m) was presented. This UAV model includes an infrared camera to detect oil leakage in pipeline networks caused by geological hazard and interference from third party. UAV CFD simulations through the ANSYS-CFX[®] software were developed to predict the lift and drag coefficients as functions of the Reynolds number and angles of attack (AoA). For an inlet velocity of 26 m/s, the maximum magnitude (0.668) of the lift coefficient of the UAV model was achieved with AoA of 18°. The lift coefficient of the UAV model increased when AoA varied from 0° to 18°. For this AoA, the drag coefficient of the UAV model registered a value of 0.080. The values of the lift coefficient decay for AoA higher than 18°. A scale model (1:6.5) of the UAV was fabricated using a 3D printer. In addition, the lift and drag coefficients were measured through a subsonic wind tunnel. For AoA of 0°, the drag coefficients obtained using the UAV CFD simulations for Reynolds number between 1.11×10^5 and 1.527×10^5 have an approximately similar behavior compared with experimental results.

The designed UAV has a suitable aerodynamic behavior that could allow its implementation for low-cost inspections of oil pipelines. The UAV could include a small infrared camera, a GPS and a communication system for real-time transmission of the infrared images related to oil leakage. The infrared camera could be located at the bottom surface of the UAV. This camera could identify by infrared radiation the oil leakages in pipelines caused by geological hazard and interference from third party. The proposed UAV could detect pipeline sections with high risks and recognize the potential failures sources. This UAV could reduce the inspection costs compared to other conventional aircrafts such as helicopters or light aircrafts.

Acknowledgements

This research was funded by *Programa Fortalecimiento de la Calidad Educativa (PFCE) 2018* through grant 30MSU0940B-21.

References

- ANSYS, Inc. (2019, November 7). ANSYS CFX-Solver Theory Guide.
- Bardina, J. E., Huang, P. G., & Coakley, T. J. (1997). Turbulence Modeling, Validation, Testing and Development. *NASA Technical Memorandum* 110446.
- Barros, S. (2016). A review of quantitative risk assessment of onshore pipelines. *Journal of Loss Prevention in the Process Industry*, 44, 282-298. doi: <https://doi.org/10.1016/j.jlp.2016.09.016>
- Bouix, R., Viot, P., & Lataillade, J. L. (2009). Polypropylene foam behaviour under dynamic loadings: Strain rate, density and microstructure effects. *International Journal of Impact Engineering*, 36(2), 329-342. doi: <https://doi.org/10.1016/j.ijimpeng.2007.11.007>
- Bravo-Mosquera, P. D., Botero-Bolivar, L., Acevedo-Giraldo, D., & Cerón-Muñoz, H. D. (2017). Aerodynamic design analysis of a UAV for superficial research of volcanic environments. *Aerospace Science and Technology*, 70, 600-614. doi: <https://doi.org/10.1016/j.ast.2017.09.005>
- Cengel, Y. A., & Cimbala, J. M. (2014). *Fluid Mechanics Fundamentals Applications*. New York: McGraw-Hill.
- Du, X., Dori, A., Divo, E., Huayamave, V., & Zhu, F. (2018). Modeling the motion of small unmanned aerial system (sUAS) due to ground collision. *Proceedings of the Institution of Mechanical Engineers Part G: Journal of Aerospace Engineering*, 232(10), 1961-1970. doi: <https://doi.org/10.1177/0954410017705903>
- Frederick, G., Kaupp, G. A., Kudelko, C. M., Schuster, P. J., Domas, F., Haardt, U. G., & Lenz, W. (1995). Optimization of expanded polypropylene foam coring to improve bumper foam core energy absorbing capability. *SAE International*, e-ISSN: 2688-3627, 1-9. doi: <https://doi.org/10.4271/950549>
- Gómez, C., & Green, D. R. (2017). Small unmanned airborne systems to support oil and gas pipeline monitoring and mapping. *Arabian Journal of Geosciences*, 10, 202. doi: <https://doi.org/10.1007/s12517-017-2989-x>
- Guo, Y., Meng, X., Wang, D., Meng, T., Liu, S., & He, R. (2016). Comprehensive risk evaluation of long-distance oil and gas transportation pipelines using a fuzzy Petri net model. *Journal of Natural Gas Science and Engineering*, 33, 18-29. doi: <https://doi.org/10.1016/j.jngse.2016.04.052>
- Iqbal, H., Tesfamariam, S., Haider, H., & Sadiq, R. (2016). Inspection and maintenance of oil & gas pipelines: A review of policies. *Structure and Infrastructure Engineering*, 13(6), 1-23. doi: <http://doi.org/10.1080/15732479.2016.1187632>
- Jung-Ryul, L., Chang, C., Chan, P., Chung, T., Hye, S., Hyomi, J., & Eric, B. F. (2015). Spar disbond visualization in in-service composite UAV with ultrasonic propagation imager. *Aerospace Science and Technology*, 45, 180-185. doi: <https://doi.org/10.1016/j.ast.2015.05.010>

- Liang, W., Hu, J., Zhang, L., Guo, C., & Lin, W. (2012). Assessing and classifying risk of pipeline third-party interference based on fault tree and SOM. *Engineering Applications of Artificial Intelligence*, 25(3), 594-608. doi: <https://doi.org/10.1016/j.engappai.2011.08.010>
- Lima, G. F., Freitas, V. C. G., Araújo, R. P., Maitelli, A. L., & Salazar, A. O. (2017). PIG's speed estimated with pressure transducers and Hall effect sensor: An industrial application of sensors to validate a testing laboratory. *Sensors*, 17(9), 2119. doi: <https://doi.org/10.3390/s17092119>
- Menter, F. R. (1993). Zonal two equation $k-\omega$ turbulence models for aerodynamic flows. *Aerospace Research Central AIAA* 93-2906. doi: <https://doi.org/10.2514/6.1993-2906>
- Menter, F., Carregal-Ferreira, J., Esch, T., & Konno, B. (2003). The SST turbulence model with improved wall treatment for heat transfer predictions in gas turbines. *Proceedings of the International Gas Turbine Congress 2003* (pp. 1-7). Tokyo, IGTC2003-TS-059.
- Enlace: <https://pdfs.semanticscholar.org/06cc/622fb262b39b3ef0eb2c266baf08a94a6f1d.pdf>
- Menter, F. R., Kuntz, M., & Langtry, R. (2003). Ten years of industrial experience with the SST turbulence model. *Turbulence, Heat and Mass Transfer*, 4, 625-632.
- Enlace: https://cfds.spbstu.ru/agarbaruk/doc/2003_Menter,%20Kuntz,%20Langtry_Ten%20years%20of%20industrial%20experience%20with%20the%20SST%20turbulence%20model.pdf
- Mohamed, A., Hamdi, M. S., & Tahar, S. (2017). Using computational intelligence for the safety assessment of oil and gas pipelines: A survey. In W. Pedrycz, & S. M. Chen (Eds.). *Data science and big data: An environment of computational intelligence. Studies in Big Data* (pp. 189-207). Springer International Publishing: Cham. doi: https://doi.org/10.1007/978-3-319-53474-9_9
- Munson, B. R., Okiishi, T. H., Rothmayer, A. P., & Huebsch, W. W. (2009). *Fundamentals of fluid mechanics* (6th Ed.). Danvers, MA: John Wiley & Sons.
- Panagiotou, P., Fotiadis-Karras, S., & Yakinthos, K. (2018). Conceptual design of a Blended Wing Body MALE UAV. *Aerospace Science and Technology*, 73, 32-47. doi: <https://doi.org/10.1016/j.ast.2017.11.032>
- Panagiotou, P., Kaparos, P., Salpingidou, C., & Yakinthos, K. (2016). Aerodynamic design of a MALE UAV. *Aerospace Science and Technology*, 50, 127-138. doi: <https://doi.org/10.1016/j.ast.2015.12.033>
- Panagiotou, P., Ioannidis, G., Tzivinikos, I., & Yakinthos, K. (2017). Experimental investigation of the wake and the wingtip vortices of a UAV model. *Aerospace*, 4(4), 53. doi: <https://doi.org/10.3390/aerospace4040053>
- Raeisi, B., & Alighanbari, H. (2018). Effects of tilting rate variations on the aerodynamics of the tilting ducted fans mounted at the wing tips of a vertical take-off and landing unmanned aerial vehicle. *Proceedings of the Institution of Mechanical Engineers, Part G: Journal of Aerospace Engineering*, 232(10), 1803-1813. doi: <https://doi.org/10.1177/0954410017703146>
- Rifai, D., Abdalla, A. N., Razali, R., Ali, K., & Faraj, M. A. (2017). An Eddy current testing platform system for pipe defect inspection based on an optimized Eddy current technique probe design. *Sensors*, 17(3), 579. doi: <https://doi.org/10.3390/s17030579>
- Rodríguez-Olivares, N. A., Cruz-Cruz, J. V., Gómez-Hernández, A., Hernández-Alvarado, R., Nava-Balanzar, L., Salgado-Jiménez, T., & Soto-Cajiga, J. A. (2018). Improvement of ultrasonic pulse generator for automatic pipeline inspection. *Sensors*, 18(9), 2950. doi: <https://doi.org/10.3390/s18092950>
- Sahli, H., & El-Sheimy, N. (2016). A novel method to enhance pipeline trajectory determination using pipeline junctions. *Sensors*, 16(4), 567. doi: <https://doi.org/10.3390/s16040567>
- Schlichting, H., & Gersten, K. (2017). *Boundary-Layer Theory*. Berlin, Germany: Springer Nature. doi: <https://doi.org/10.1007/978-3-662-52919-5>
- Shen, J., Su, Y., Liang, Q., & Zhu, X. (2018). Calculation and identification of the aerodynamic parameters for small-scaled fixed-wing UAVs. *Sensors*, 18(1), 206. doi: <https://doi.org/10.3390/s18010206>

- Shukla, D., & Komerath, N. (2018). Multirotor drone aerodynamic interaction investigation. *Drones*, 2(4), 43. doi: <https://doi.org/10.3390/drones2040043>
- Shu-Jiao, T., Zong-Zhi, W., Ru-Jun, W., & Hao, W. (2016). Fire risk study of long-distance oil and gas pipeline based on QRA. *Procedia Engineering*, 135, 369-375. doi: <https://doi.org/10.1016/j.proeng.2016.01.144>
- Sóbestor, A., Keane, A., Scanlan, J., & Bressloff, N. (2005). Conceptual design of UAV airframes using a generic geometry service. In *Proceedings of the Infotech@Aerospace Conferences* (pp. 26-29). Arlington, VA, USA. doi: <https://doi.org/10.2514/6.2005-7079>
- Yang, F., Xue, X., Cai, C., Sun, Z., & Zhou, Q. (2018). Numerical simulation and analysis on spray drift movement of multirotor plant protection unmanned aerial vehicle. *Energies*, 11(9), 2399. doi: <https://doi.org/10.3390/en11092399>
- Yuhua, D., & Datao, Y. (2005). Estimation of failure probability of oil and gas transmission pipelines by fuzzy fault tree analysis. *Journal of Loss Prevention in the Process Industries*, 18(2), 83-88. doi: <https://doi.org/10.1016/j.jlp.2004.12.003>
- Zhou, Q., Wu, W., Liu, D., Li, K., & Qiao, Q. (2016). Estimation of corrosion failure likelihood of oil and gas pipeline based on fuzzy logic approach. *Engineering Failure Analysis*, 70, 48-55. doi: <https://doi.org/10.1016/j.engfailanal.2016.07.014>